Chaos, Solitons and Fractals 212 (2026) 119026

Contents lists available at ScienceDirect

Chaos, Solitons and Fractals

journal homepage: www.elsevier.com/locate/chaos

Bounded random perturbations in chaotic systems with intermingled basins of attraction

Vitor H.A. Fávaro [a,*], Bruno M. Czajkowski [a], Ricardo L. Viana [a,b]

[a] Universidade Federal do Paraná, Departamento de Física, Curitiba, Paraná, Brazil
[b] Universidade Federal do Paraná, CICTI, NCC, Curitiba, Paraná, Brazil

ARTICLE INFO

Keywords:
Riddled basins
Kan's model
Coupled Lorenz-like system
Modeling uncertainty
Invariant manifolds
Intermittent behavior

ABSTRACT

This work investigates how bounded modeling uncertainties affect systems with intermingled basins. We analyze two systems, a modified Kan map and a coupled Lorenz-like system, both of which exhibit intermingled basin structures. A bounded random perturbation, representing modeling uncertainty, is introduced, and proximity to invariant sets is measured through a numerical tolerance. By varying the perturbation over twelve orders of magnitude and considering different tolerance values, we show that the dynamics are primarily organized by the ratio between perturbation amplitude and classification tolerance, rather than by their absolute values. For small ratios, trajectories remain near invariant sets; for intermediate values, residence times collapse; and for large ratios, trajectories are expelled from invariant neighborhoods. In the coupled Lorenz-like system, synchronized states decay smoothly as uncertainty increases, whereas antisynchronized states break down abruptly. Overall, both models display the same sequence of dynamical regimes, suggesting that this sensitivity mechanism is robust across different dynamical structures.

1. Introduction

Chaotic dynamics constrained by invariant subspaces often involve a competition between attraction along the subspace and instability in transverse directions [1,2]. In many systems, chaotic attractors embedded in such manifolds can be transversely stable on average while still containing transversely unstable periodic orbits. This coexistence gives rise to intermittent bursts that drive trajectories away from the subspace, producing a delicate balance between confinement and escape [3–5]. As a consequence, trajectories starting arbitrarily close to one another may evolve toward different asymptotic states, reflecting an extreme sensitivity to initial conditions [1,6].

When this mechanism operates in the presence of multiple invariant subspaces, each supporting a different attractor, the geometry of the associated basins can become highly intricate [7,8]. In particular, the basins may fail to organize into well-separated regions and instead interpenetrate at arbitrarily fine scales, leading to riddled or intermingled structures [1,6,9,10]. Riddled basins correspond to situations in which one basin is densely perforated by another [11–16], whereas intermingled basins represent a configuration in which both basins are densely intertwined [8,17–19]. In this regime, every neighborhood of the phase space contains points converging to different attractors, regardless of how small the region is chosen [9,18,19]. Such structures have been extensively reported in different classes of dynamical systems, indicating their robustness across distinct modeling frameworks [17,20–32].

* Corresponding author.
E-mail address: vitor.favaro@ufpr.br (V.H.A. Fávaro).

https://doi.org/10.1016/j.chaos.2026.119026
Received 13 May 2026; Received in revised form 24 July 2026; Accepted 19 August 2026
Available online 29 August 2026
0960-0779/© 2026 The Authors. Published by Elsevier Ltd. This is an open access article under the CC BY license (http://creativecommons.org/licenses/by/4.0/).

From the standpoint of predictability, these basin structures impose severe limitations [18,19]. Unlike standard fractal basin boundaries, where predictability can improve as resolution increases [6], intermingled basins may retain uncertainty even arbitrarily close to the attracting invariant set, so reducing measurement uncertainty does not necessarily restore a well-defined outcome [7,8]. Because arbitrarily small perturbations can redirect trajectories toward different attractors, unpredictability becomes an intrinsic feature of the phase space rather than a consequence of limited precision [1].

Despite this extensive body of work, most studies implicitly assume that the governing equations are exactly known and that invariant sets can be sharply identified [4,10]. In realistic modeling scenarios, however, this assumption is rarely satisfied. Dynamical systems are typically affected by uncertainties arising from imperfect parameter estimation, unresolved processes, measurement noise, and numerical discretization [33,34]. These factors introduce persistent discrepancies between the mathematical model and the underlying dynamics, often referred to as modeling errors [35–37]. Moreover, invariant sets cannot be identified exactly in numerical or experimental settings, but only up to a finite tolerance, which effectively introduces an additional scale associated with observational or computational resolution.

The coexistence of intrinsic dynamical sensitivity and external modeling uncertainty is particularly relevant in systems with intermingled basins. Because different asymptotic behaviors are already densely distributed, even small modeling errors can produce macroscopic changes in the observed outcome. This naturally leads to a two-parameter description involving both the perturbation amplitude and the tolerance used to classify trajectories relative to invariant sets.

This behavior contrasts with that of standard bistable systems. In such systems, bounded perturbations induce transitions only when trajectories leave locally stable neighborhoods surrounding each attractor and approach well-defined basin boundaries, so that escape events can be understood as rare threshold crossings governed primarily by geometric distance to the boundary. In this regime, the internal organization of the basin away from the boundary plays essentially no role in the dynamics under small perturbations.

By contrast, intermingled basins contain points that converge to different attractors in every neighborhood of the phase space. Consequently, arbitrarily small perturbations may bring trajectories into regions associated with different asymptotic outcomes. One may therefore expect the response to bounded perturbations to be strongly influenced by the geometry of the intermingled basin structure rather than solely by the distance to a localized boundary.

In this work, we investigate how bounded modeling uncertainties affect dynamical systems with intermingled basin structures, focusing on the interplay between the perturbation amplitude ε and the tolerance δ used to define proximity to invariant sets. To investigate these effects, we examine two representative systems, namely a minimal discrete-time map and a higher-dimensional continuous-time system. As a first example, we analyze a modified version of Kan's map [18], which possesses two chaotic invariant sets with intermingled basins. As a higher-dimensional continuous-time counterpart, we study a coupled Lorenz-like system [38,39], whose synchronized and antisynchronized invariant manifolds play a role analogous to the invariant sets of the map.

By systematically varying ε and δ over several orders of magnitude, we show that the observable dynamics is governed by the ratio between their scales. When $\varepsilon \ll \delta$, trajectories remain effectively confined to invariant neighborhoods; as ε approaches δ, residence times collapse and intermittent switching becomes most active; and when $\varepsilon \gg \delta$, trajectories spend most of their time outside all invariant sets. This phenomenology is robust across both systems, indicating that the balance between perturbation amplitude and classification scale, rather than either quantity alone, controls the effective structure of intermingled basins under modeling uncertainty.

The paper is organized as follows. In Section 2, we introduce a modified version of Kan's map and present the corresponding numerical results, focusing on how bounded random perturbations and classification tolerances affect the intermingled basin structure. In Section 3, we extend the analysis to a coupled Lorenz-like system, where we again present both the model and its numerical results, demonstrating that the same organizing mechanism persists in a higher-dimensional continuous-time setting. Finally, the last Section is devoted to our Conclusions.

2. Modified version of Kan's model

A family of two-dimensional discrete-time models for competing species was introduced by Hofbauer et al. [40]. In this formulation, the populations $x_1(n)$ and $x_2(n)$ evolve under symmetric update rules chosen so that the ratio between the species and the total population satisfies biologically motivated constraints [41,42]. Introducing the variables

$$x = x_1 + x_2, \qquad y = \frac{x_1}{x}, \tag{1}$$

the dynamics can be written as the map

$$x_{n+1} = T(x_n), \tag{2}$$

$$y_{n+1} = y_n + \kappa\, y_n(1 - y_n)\, g(x_n), \tag{3}$$

where x_{n+1} stands for the total population, y_{n+1} governs the fraction of species 1, $T(x_n)$ determines the evolution of the total population, and $g(x_n)$ modulates the interaction between the two species. This model contains two invariant subspaces defined as

$$I_0 = \{(x, y) \in [0, 1] \mid y = 0\}, \tag{4}$$

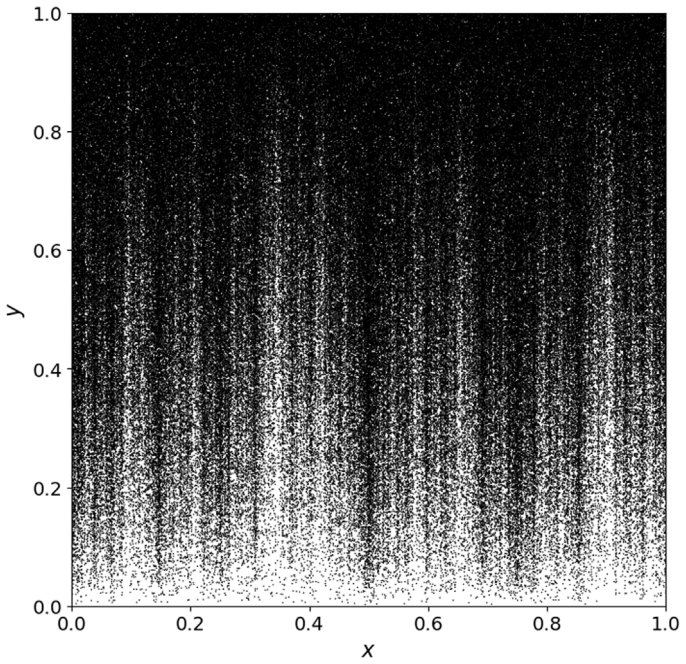


Fig. 1. Basins of attraction for the invariant sets I_0 (white) and I_1 (black) for the modified Kan's model with $\kappa = 0.3$.

and

$$I_1 = \{(x, y) \in [0, 1] \mid y = 1\}, \tag{5}$$

corresponding to states in which only one species persists, each containing an attractor.

Kan previously analyzed a particular case defined by $T(x) = 3x \mod 1$ and $g(x) = \cos(2\pi x)$, proving the existence of intermingled basins for $\kappa = 1/32$ [9]. Subsequent work by Hofbauer et al. [40] extended this result to broader parameter regimes $0 < \kappa < 1$. In the present paper, we consider a modified version of Kan's model [18], given by

$$x_{n+1} = 4x_n(1 - x_n), \tag{6}$$

$$y_{n+1} = y_n + \kappa y_n(1 - y_n)\cos(3\pi x_n). \tag{7}$$

To illustrate the intermingled basin structure of the modified Kan map, Fig. 1 shows the basins of attraction associated with the invariant sets I_0 ($y = 0$) and I_1 ($y = 1$) for $\kappa = 0.3$. The white and black regions correspond to initial conditions that converge to I_0 and I_1, respectively. The dense intermingling of the two basins implies that every neighborhood in phase space contains initial conditions converging to both invariant sets.

We introduce a bounded random perturbation, representing modeling uncertainty, into the transversal dynamics in order to investigate how modeling uncertainties deform the intermingled basin structure. The perturbed map is defined as

$$x_{n+1} = 4x_n(1 - x_n), \tag{8}$$

$$y_{n+1} = y_n + \kappa y_n(1 - y_n)\cos(3\pi x_n) + \varepsilon\, \sigma_n\, \sin(x_n - y_n), \tag{9}$$

where $\varepsilon \ll \kappa$ specifies the amplitude of the perturbation and σ_n is an independent random variable drawn from the uniform distribution on $[0, 1]$ at each iteration n. The sinusoidal factor is chosen as a generic, smooth, bounded function capable of representing a wide class of modeling errors while ensuring that the perturbation remains within $[-\varepsilon, \varepsilon]$. Because the perturbation is added through a single equation shared by both invariant sets, any bounded, state-dependent function of this kind affects I_0 and I_1 symmetrically, so the qualitative results reported here do not depend on this particular choice. Unbounded noise sources (such as Gaussian or Lorentzian distributions) were not considered because they may generate arbitrarily large perturbations, which fall outside the modeling assumptions adopted in this work.

Since numerical trajectories never satisfy $y = 0$ or $y = 1$ exactly, proximity to the invariant sets is determined through a tolerance parameter δ, according to the criteria

$$\begin{cases} I_0, & \text{if } y < \delta, \\ I_1, & \text{if } 1 - y < \delta, \end{cases} \tag{10}$$

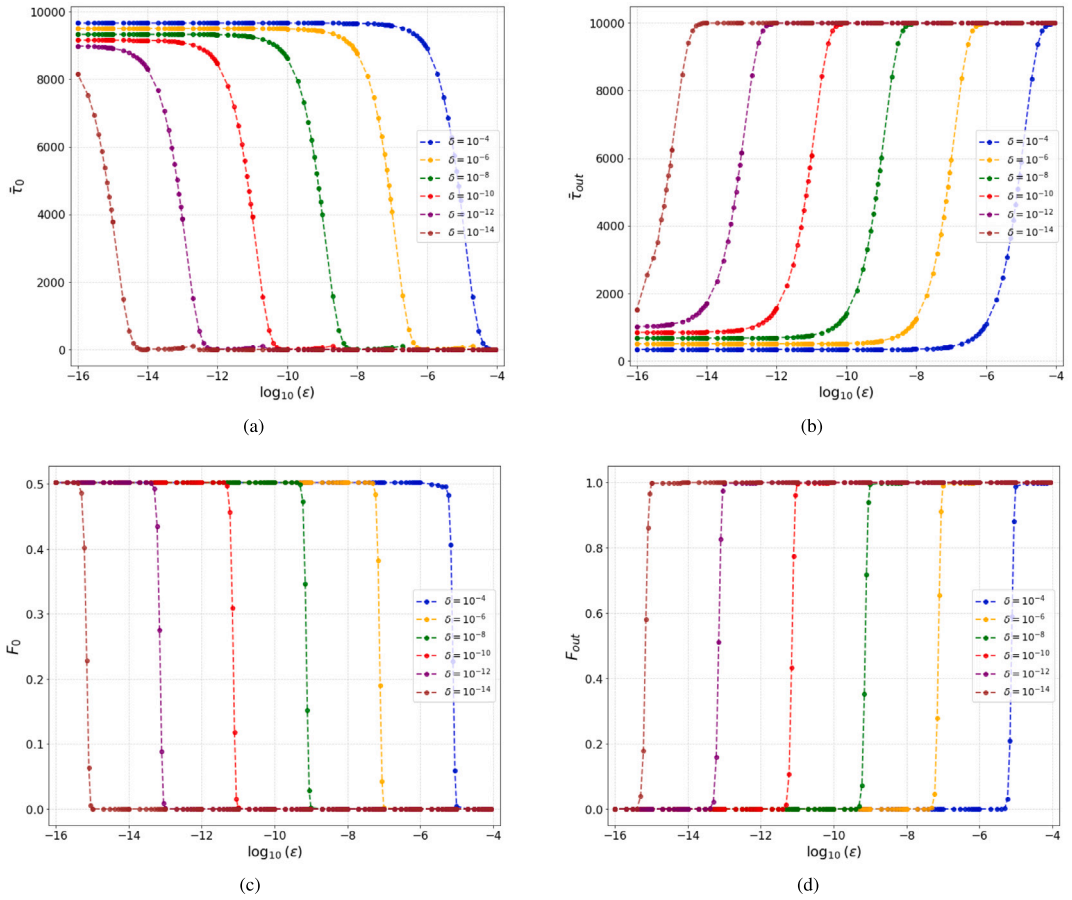


Fig. 2. (a) Mean residence time $\bar{\tau}_0$ in I_0 and (b) mean residence time $\bar{\tau}_{out}$ outside both invariant sets, as functions of the modeling error ε. Panels (c) and (d) show the corresponding fractions F_0 and F_{out} of initial conditions assigned to I_0 and to the region outside both invariant sets, respectively. Each curve corresponds to a different value of δ, highlighting the dependence on both the perturbation amplitude and the classification tolerance. All panels correspond to $\kappa = 0.3$.

with all remaining points classified as outside both neighborhoods. We investigate the influence of this threshold by varying δ over the values 10^{-14}, 10^{-12}, 10^{-10}, 10^{-8}, 10^{-6}, and 10^{-4}. Similarly, the model uncertainty ε is varied across twelve orders of magnitude, from 10^{-16} to 10^{-4}. For each pair (ε, δ), the map is iterated for $T = 10^4$ steps starting from a uniform 100×100 grid of initial conditions in $(x, y) \in [0, 1] \times [0, 1]$.

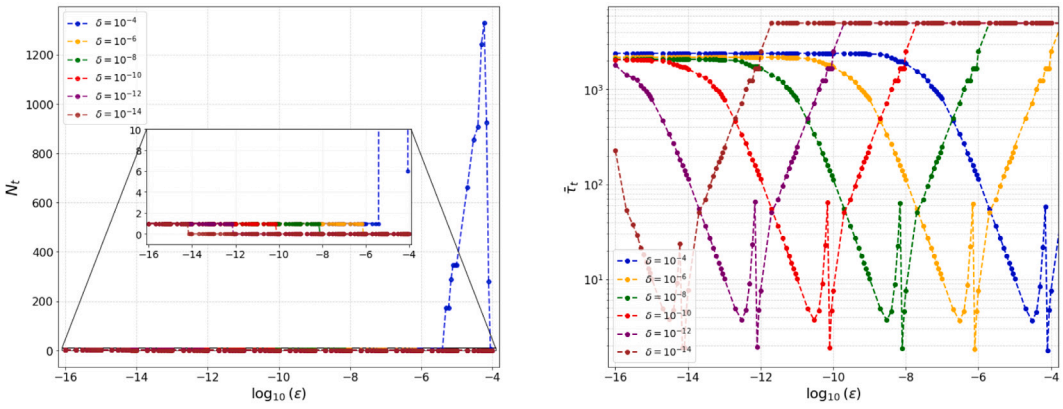
To quantify how trajectories distribute among the neighborhoods of the invariant sets and the region outside them, we compute, for each pair ε and δ, the mean residence times $\bar{\tau}_0$, $\bar{\tau}_1$, and $\bar{\tau}_{out}$, defined as the average durations of the time intervals during which the trajectory remains within the δ-neighborhoods of I_0, I_1, or outside both. In parallel, we evaluate, over the full ensemble of initial conditions, the corresponding fractions F_0, F_1, and F_{out}, obtained by identifying the region each trajectory occupies for more than half of the total observation time. These quantities are computed independently, and the fractions satisfy $F_0 + F_1 + F_o = 1$. Their dependence on the modeling error ε, for several values of δ, is shown in Fig. 2.

Due to the symmetry of the map, the invariant sets I_0 and I_1 exhibit identical qualitative behavior under the perturbation. Accordingly, in the following we present results only for I_0, while the corresponding results for I_1 are omitted for brevity.

The mean residence time $\bar{\tau}_0$ of trajectories classified as belonging to I_0 is presented in Fig. 2(a). For small ε, the curves associated with larger tolerances remain close to the maximal observation time, while the strictest threshold ($\delta = 10^{-14}$) already exhibits a noticeable decrease at the smallest perturbation considered. As ε grows, all curves undergo a sharp decline once the perturbation becomes roughly two orders of magnitude smaller than the corresponding threshold, for example at $\varepsilon \sim 10^{-14}$ when $\delta = 10^{-12}$. The residence time then reaches its minimum near $\varepsilon \approx \delta$ and does not recover for larger perturbations.

A complementary view comes from the mean time spent outside both invariant sets, shown in Fig. 2(b). For weak perturbations, this time remains small compared to the residence times within the invariant sets. As ε grows, the outside both invariant sets time increases, and for sufficiently large ε, it reaches a high plateau that is largely insensitive to the choice of tolerance.

As shown in Fig. 2(c), the fraction of points assigned to I_0 indicates that for small values of ε, roughly half of the initial conditions remain near this invariant set. Once ε becomes about one order of magnitude larger than the tolerance δ (e.g., $\varepsilon = 10^{-13}$ for $\delta = 10^{-14}$), this fraction undergoes a sharp decline and reaches its minimum without recovering for larger perturbations.



(a) (b)

Fig. 3. Panel (a) shows the number of transitions N_t between I_0 and I_1, and (b) displays the average intermittent transition duration $\bar{\tau}_t$. All panels are plotted as functions of the perturbation intensity ε for different classification thresholds δ, with $\kappa = 0.3$.

The resulting redistribution appears in Fig. 2(d), where the fraction outside both invariant sets increases precisely in the region where the curves in panel (c) collapse, demonstrating that points leaving the neighborhood of I_0 do not transition to I_1, and vice versa; instead, they move to the region outside both invariant sets. For sufficiently large ε, this fraction approaches 1.0, indicating that all initial conditions spend more than half of their time away from the neighborhoods of both invariant sets.

To complement the residence-time analysis and the classification of initial conditions into I_0, I_1, or the region outside both, we also characterize the temporal structure of the switching dynamics. For each trajectory, we count the total number of transitions N_t between the neighborhoods of I_0 and I_1. In addition, we compute the average intermittent transition duration $\bar{\tau}_t$, defined as the mean time interval separating consecutive visits to these neighborhoods.

Importantly, this interval is computed regardless of whether the trajectory switches directly from I_0 to I_1 (or vice versa). The trajectory may temporarily leave a neighborhood, evolve for some time in the region outside both I_0 and I_1, and subsequently return to the same neighborhood. In such cases, the duration of this excursion also contributes to $\bar{\tau}_t$. Thus, $\bar{\tau}_t$ captures not only full switching events between I_0 and I_1, but also the intermittent departures and returns driven by the fluctuations induced by the interplay between ε and δ. The behavior of N_t and $\bar{\tau}_t$ is summarized in Fig. 3.

The number of transitions N_t remains low for all tolerances when $\varepsilon \ll \delta$, as visible in Fig. 3(a). The inset confirms that even the weakest perturbations generate occasional switches between I_0 and I_1. As ε increases and approaches the scale of the tolerance, all curves undergo a sudden decline, indicating that returns to the neighborhoods of I_0 and I_1 become increasingly infrequent once ε is of the same order as δ. A distinct behavior appears for the most permissive threshold $\delta = 10^{-4}$, in which N_t begins to rise markedly around $\varepsilon \sim 10^{-5}$, continues to increase over a finite interval, and only later decreases as the perturbation grows further. Overall, the figure reveals a coherent pattern in which transitions remain rare when ε is much smaller than δ, although still present, and disappear entirely once ε reaches the classification threshold.

Additional insight comes from the behavior of $\bar{\tau}_t$, displayed in Fig. 3(b). For perturbations much smaller than the tolerance δ, $\bar{\tau}_t$ remains large, a behavior that persists while ε is roughly five orders of magnitude below δ. As the gap decreases to about four orders of magnitude, $\bar{\tau}_t$ begins to fall. Each curve reaches its minimum when ε becomes comparable to δ, which coincides with the point where Fig. 3(a) shows the smallest values of N_t. Once this region is crossed, $\bar{\tau}_t$ increases again for nearly two further orders of magnitude in ε and eventually settles into a plateau, for example around $\varepsilon = 10^{-8}$ when $\delta = 10^{-10}$.

Across all diagnostics, a consistent pattern emerges. For $\varepsilon \ll \delta$, trajectories remain close to one of the invariant sets I_0 or I_1. As the perturbation increases and becomes only a few orders of magnitude smaller than the tolerance, for example, when $\varepsilon \approx 10^{-12}$ while $\delta = 10^{-10}$, the dynamics become most active. For larger perturbations, once ε approaches or exceeds the scale of δ, trajectories are pushed predominantly into the region outside both invariant sets, causing the residence times in I_0 and I_1 to collapse and the out-of-basin intervals to dominate. In this way, these results show how the balance between ε and δ regulates access to the neighborhoods of the invariant sets.

Having characterized how modeling uncertainty restructures the dynamics in this two-dimensional map, we now examine whether the same organizing mechanism persists in a higher-dimensional continuous-time system. For this purpose, we turn to a six-dimensional coupled Lorenz-like model whose synchronized and antisynchronized manifolds also exhibit intermingled basins.

3. Coupled Lorenz-like system

The Lorenz system is a classical model in nonlinear dynamics, originally introduced to study atmospheric convection [43,44]. Several variants of the Lorenz equations have been proposed to simplify specific nonlinearities while preserving the essential

structure of its double-wing chaotic attractor [19,39,45–51]. Among them, Elwakil et al. [38] introduced a piecewise-linear Lorenz-like model defined by

$$\frac{d\tilde{x}}{dt} = a(\tilde{y} - \tilde{x}), \tag{11}$$

$$\frac{d\tilde{y}}{dt} = s\,k(\tilde{x})\tilde{z} + m, \tag{12}$$

$$\frac{d\tilde{z}}{dt} = -s|\tilde{x}| + s, \tag{13}$$

where a, m, and s are system parameters. The switching function

$$k(\tilde{x}) = \begin{cases} 1, & \tilde{x} \geq 0, \\ -1, & \tilde{x} < 0, \end{cases} \tag{14}$$

replaces the nonlinear product $\tilde{x}\tilde{y}$ in the original Lorenz equations, producing a piecewise-linear dynamics reminiscent of Chua-type systems. To avoid discontinuities at $\tilde{x} = 0$, one may replace $k(\tilde{x})$ with the smooth approximation $\tanh(c\tilde{x})$ for $c \gg 1$. With this modification, the model becomes

$$\frac{d\tilde{x}}{dt} = a(\tilde{y} - \tilde{x}), \tag{15}$$

$$\frac{d\tilde{y}}{dt} = \tilde{z}\tanh(c\tilde{x}) + m, \tag{16}$$

$$\frac{d\tilde{z}}{dt} = -|\tilde{x}| + 1, \tag{17}$$

which retains the two-wing chaotic attractor for $a = 0.5$, $m = 0$, and $c = 50$, with fixed points at $(\pm 1, \pm 1, 0)$.

In this work we consider two identical copies of the smoothed Lorenz-like system coupled through their z variables [39]:

$$\frac{dx_i}{dt} = a(y_i - x_i), \tag{18}$$

$$\frac{dy_i}{dt} = z_i\tanh(cx_i) + m, \tag{19}$$

$$\frac{dz_i}{dt} = -|x_i| + 1 + \kappa(z_j - z_i), \tag{20}$$

for $i, j \in \{1, 2\}$ with $i \neq j$. The coupling strength κ controls the interaction between the z components.

The symmetry of the coupled equations naturally gives rise to two three-dimensional invariant manifolds that organize the dynamics [39]. The first of these is the synchronized manifold, defined as

$$M_S = \{(v_1, v_2) \in \mathbb{R}^6 \mid x_1 = x_2,\ y_1 = y_2,\ z_1 = z_2\}, \tag{21}$$

and the second is the antisynchronized manifold, given by

$$M_A = \{(v_1, v_2) \in \mathbb{R}^6 \mid x_1 = -x_2,\ y_1 = -y_2,\ z_1 = z_2\}, \tag{22}$$

where $v_i = (x_i, y_i, z_i)$ denotes the state of each subsystem. For weak coupling ($\kappa \lesssim 0.10$) both manifolds are transversely unstable, so trajectories do not remain close to them over long times [39]. To ensure that M_S and M_A play a dynamically relevant role in the evolution of the system, we focus on coupling strengths $\kappa \geq 0.15$ throughout this work.

To illustrate the basin structure of Eqs. (18)–(20), Fig. 4 displays the basins of attraction for $\kappa = 0.41$. The white and black regions represent sets of initial conditions that asymptotically converge to the synchronized (M_S) and antisynchronized (M_A) manifolds, respectively.

To investigate the impact of modeling errors, we introduce a bounded random perturbation into the coupled Lorenz-like system. The perturbed system is written as

$$\frac{dx_i}{dt} = a(y_i - x_i), \tag{23}$$

$$\frac{dy_i}{dt} = z_i\tanh(cx_i) + m, \tag{24}$$

$$\frac{dz_i}{dt} = -|x_i| + 1 + \kappa(z_j - z_i) + \varepsilon\,\sigma\,\sin(x_i - z_i), \tag{25}$$

where $\varepsilon \ll \kappa$ represents the modeling uncertainty and σ is a random variable uniformly distributed in $[0, 1]$. The term $\sin(x_i - z_i)$ is adopted as a generic smooth bounded perturbation representing state-dependent fluctuations. As in Eqs. (8) and (9), bounded random perturbations are essential to maintain physical plausibility by ensuring that the perturbation amplitude remains controlled by ε. In the present system, however, whether the perturbation respects the coupling symmetry between the two subsystems also determines which invariant manifolds are preserved by the perturbed dynamics. The chosen perturbation preserves the synchronized manifold M_S but does not preserve the antisynchronized manifold M_A. The dynamical consequences of this distinction are discussed later in this section.

The perturbed system is analyzed numerically using the parameters $a = 0.5$, $c = 50$, $m = 0$, and a coupling strength of $\kappa = 0.41$. The same range of modeling uncertainty ε employed in the study of Eqs. (8) and (9) is adopted here. To examine whether the

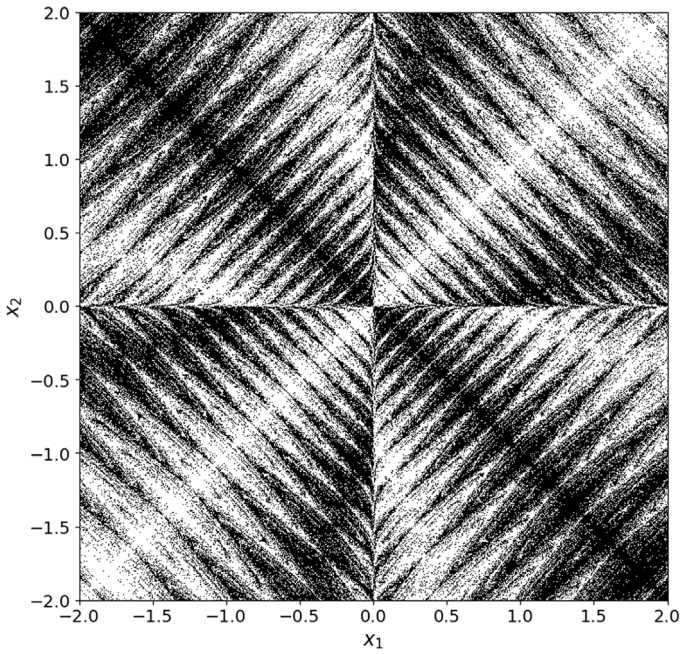


Fig. 4. Basins of attraction for the synchronized manifold M_S (white) and the antisynchronized manifold M_A (black) in the coupled Lorenz-like system defined by Eqs. (18)–(20), for $\kappa = 0.41$. Initial conditions: x_1 and x_2 are sampled over $[-2, 2]$ on a 1000×1000 uniform grid, with $y_1 = y_2 = 0$ and $z_1 = z_2 = 2.0$.

qualitative behavior depends on the region of the phase space being sampled, an initial condition grid is considered where x_1 and x_2 vary over $[-2, 2]$ on a 100×100 grid, with $y_1 = y_2 = 0$ and $z_1 = z_2 = 2.0$. Each point is integrated up to $T = 10^4$.

Analogously to the classification adopted for the invariant sets I_0 and I_1 in the modified Kan map, we identify proximity to the synchronized manifold M_S whenever

$$|x_1 - x_2| < \delta, \qquad |y_1 - y_2| < \delta, \qquad |z_1 - z_2| < \delta, \tag{26}$$

and proximity to the antisynchronized manifold M_A whenever

$$|x_1 + x_2| < \delta, \qquad |y_1 + y_2| < \delta, \qquad |z_1 - z_2| < \delta. \tag{27}$$

Exact equality cannot be achieved numerically, so δ defines the classification scale. Points satisfying neither condition are labeled as outside both manifolds.

To quantify how trajectories distribute themselves among the neighborhoods of M_S, M_A, and the outside region, we compute the mean residence times $\bar{\tau}_S$, $\bar{\tau}_A$, and $\bar{\tau}_{out}$ for each pair (ε, δ). In parallel, for the ensemble of initial conditions we determine the corresponding fractions of points F_S, F_A, and F_{out}, according to which region each trajectory occupies for more than half of the integration time. These fractions necessarily satisfy $F_S + F_A + F_o = 1$.

We begin by examining how the perturbation intensity ε and the classification tolerance δ affect the residence times near the synchronized and antisynchronized manifolds. Fig. 5 summarizes the dependence of $\bar{\tau}_S$, $\bar{\tau}_A$, and $\bar{\tau}_{out}$ on ε for several values of δ.

The synchronized manifold remains dominant over a wide range of perturbation intensities, as displayed in Fig. 5(a). For $\log_{10}(\varepsilon) \lesssim -6$, all curves are nearly flat across different classification thresholds δ, indicating that weak perturbations do not induce deviations large enough to challenge any of the criteria used to identify synchrony. As ε increases, permanence on the manifold decreases smoothly, with stricter thresholds exhibiting earlier departures. This hierarchy reflects how perturbations progressively displace the trajectory from increasingly narrow neighborhoods of the synchronized state.

A similar structure appears in Fig. 5(b), but the loss of permanence on the antisynchronized manifold is sharper. For small ε, the system remains consistently antisynchronized for all thresholds. However, once the perturbation grows to the vicinity of the corresponding classification tolerance, typically around $\varepsilon \approx \delta$, each curve exhibits a rapid, threshold-ordered drop. This abrupt decline indicates that antisynchronization, while robust under weak perturbations, becomes considerably more brittle once ε approaches the scale at which deviations are no longer masked by the tolerance used to define proximity to the manifold.

The fraction of time spent outside both manifolds, depicted in Fig. 5(c), is negligible when ε is small, confirming that the dynamics lie predominantly near structured invariant sets. For sufficiently large perturbations, the curves converge toward a high plateau, indicating that the system spends most of the time outside both manifolds. This behavior explains the trends observed in Fig. 5(a) and (b), which include a slight but systematic reduction in the residence time on the synchronized manifold, and the near-complete

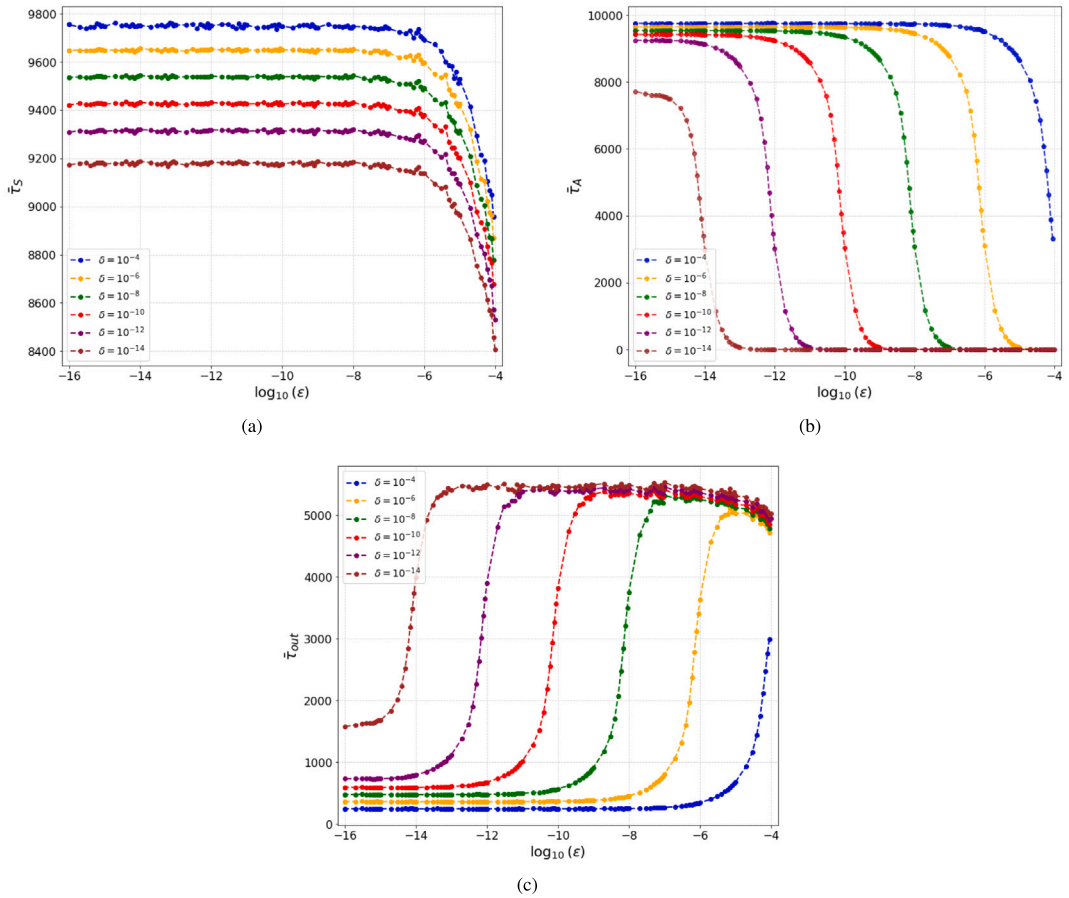


Fig. 5. Residence times in the synchronized manifold $\bar{\tau}_S$ (a), the antisynchronized manifold $\bar{\tau}_A$ (b), and outside both manifolds $\bar{\tau}_{out}$ (c) as functions of the modeling error ε, with $\kappa = 0.41$ in all panels. Each curve corresponds to a distinct value of δ, showing how residence times depend simultaneously on the perturbation amplitude and on the tolerance used to classify proximity to the manifolds. The results were obtained by fixing y_1, y_2, z_1, z_2, and varying x_1 and x_2.

suppression of permanence on the antisynchronized manifold for large ε. In this regime, successive kicks of high intensity continually displace the trajectory away from either invariant set, so that the dynamics become dominated by excursions that lie outside both manifolds.

The qualitative behavior described above is robust under variations of the coupling strength κ and persists across different choices of initial conditions and grid resolutions. We have also performed simulations in other parameter regimes, including $\kappa = 1.00$, where the invariant manifolds exhibit stronger transverse stability, as reflected by a smaller maximal transverse Lyapunov exponent than for $\kappa = 0.41$ (see Fig. 4 in Ref. [39]). In all cases, we observe the same phenomenological dependence on ε and δ. Although the numerical values of the residence times change, particularly their absolute magnitude and the precise location of the transition between regimes, the overall qualitative structure of the curves remains unchanged. For this reason, the additional plots are omitted.

Having characterized the residence times, we now turn to the fractions of initial conditions assigned to synchronization, antisynchronization, or to the region outside both manifolds. The dependence of F_S, F_A, and F_{out} on the modeling error ε and tolerance δ is summarized in Fig. 6.

The fraction of points classified on the synchronization manifold, shown in Fig. 6(a), remains nearly constant for small perturbations, with only mild fluctuations across all tolerance thresholds. As ε increases, this fraction grows slightly, but this should not be interpreted as an effective strengthening of attraction to M_S. Rather, as will be clarified below, the relative increase results from the progressive loss of points from the antisynchronized manifold.

The redistribution becomes clear in Fig. 6(b), where the fraction near M_A decreases sharply once the perturbation reaches the same order of magnitude as the tolerance threshold, that is, when $\varepsilon \approx \delta$. In this case, the fraction approaches zero in these neighborhoods and remains zero for all larger perturbations. This behavior mirrors the residence time results of Fig. 5(b), where the time spent on M_A collapses to zero once the modeling error ε becomes comparable to the classification tolerance. Considering both measures, the fraction of initial conditions and the residence time, M_A displays a distinctive fragility to increasing modeling error.

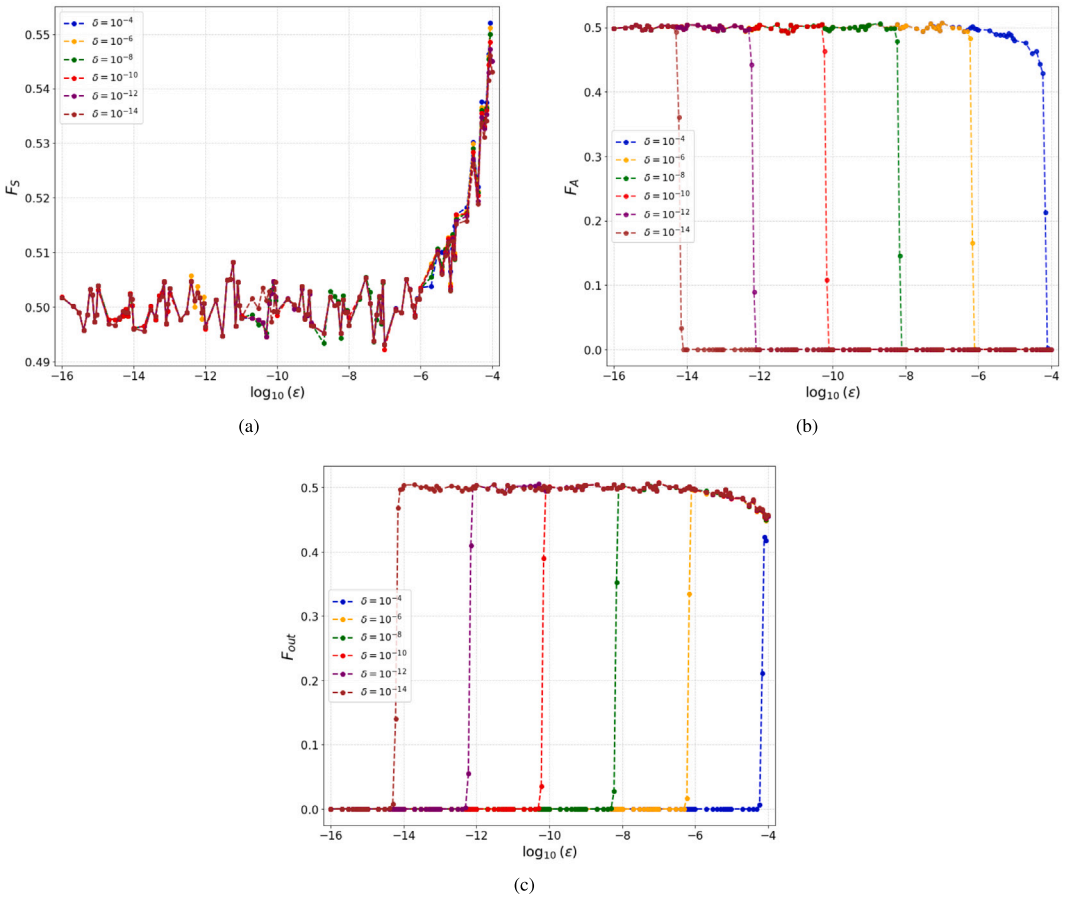


Fig. 6. Fraction of initial conditions (over a total of 10^4) whose trajectories converge to the synchronized manifold F_S (a), the antisynchronized manifold F_A (b), or remain outside both manifolds F_{out} (c), shown as a function of the modeling error ε, with $\kappa = 0.41$ in all panels. Each curve corresponds to a distinct value of δ, emphasizing how the classification depends simultaneously on the perturbation amplitude and on the tolerance used to determine proximity to the manifolds.

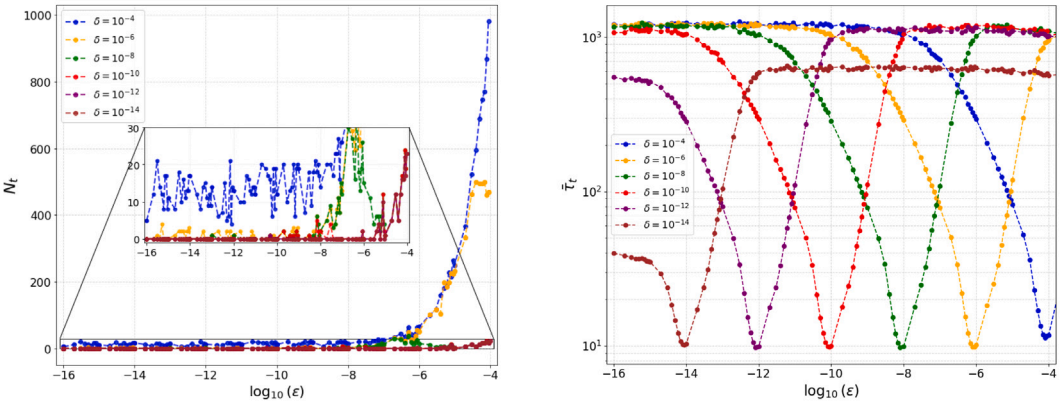
This fragility can be understood analytically by examining how the perturbation term $\varepsilon\,\sigma\sin(x_i - z_i)$ acts on the system's symmetries. On the synchronized manifold M_S (where $x_1 = x_2$, $y_1 = y_2$, $z_1 = z_2$), the perturbation terms added to both subsystems are strictly equal, preserving the synchronization condition. In contrast, on the antisynchronized manifold M_A (defined by $x_1 = -x_2$, $y_1 = -y_2$, $z_1 = z_2$), the perturbation fails to respect the antisymmetry of the manifold.

Because this antisymmetry is not preserved, the perturbation introduces a component perpendicular to M_A, acting as a transverse forcing. When the perturbation amplitude ε becomes comparable to the classification threshold δ, this transverse component rapidly pushes trajectories away from M_A, explaining the sharp collapse observed in both the residence times and the fraction of initial conditions, whereas the invariant nature of M_S under the perturbation allows it to degrade more gradually.

This interpretation is not restricted to the sinusoidal perturbation considered here. More generally, a perturbation preserves an invariant manifold only if it respects the symmetry required by that manifold, so that the perturbed vector field remains tangent to it. To verify this symmetry criterion, we replaced $\sin(x_i - z_i)$ with several qualitatively different perturbation forms, including a bounded hyperbolic tangent, an unbounded linear function, uncorrelated Gaussian noise, and perturbations with reversed or antisymmetric coupling structure. In every case, the manifold that loses persistence is exactly the one predicted by the corresponding symmetry condition, regardless of the specific functional form. Since all these cases produce the same qualitative behavior, we do not include the corresponding results here.

The behavior of the outside region, depicted in Fig. 6(c), confirms this trend. As ε grows, an increasing fraction of initial conditions becomes classified as lying outside both manifolds. The rise in this fraction occurs precisely where the curves in panel (b) collapse, indicating that trajectories initially attracted to M_A are expelled from its neighborhood and reassigned to the outside region. In other words, the perturbation does not redirect these trajectories toward synchronization but instead prevents them from remaining close to either invariant structure.

The qualitative behavior described above is robust with respect to variations in the coupling strength κ. We performed additional simulations for other parameter regimes, including $\kappa = 1.00$, where the invariant manifolds exhibit stronger transverse stability,



(a) (b)

Fig. 7. Number of transitions between the synchronized and antisynchronized manifolds N_t (a), and average intermittent transition duration $\bar{\tau}_t$ (b), shown as functions of the modeling error ε, with $\kappa = 0.41$. Each curve corresponds to a distinct value of the classification threshold δ.

as well as for different sets of initial conditions and grid resolutions. We found that the robust dependence on ε and δ remains unchanged. While the distribution of time spent in each manifold is affected, leading to a larger fraction of trajectories remaining in the synchronized manifold for stronger transverse stability, the overall phenomenology is preserved. For this reason, the corresponding figures are omitted for brevity.

To complement the residence time and fraction analyses, we also characterize the temporal structure of switching between the synchronized and antisynchronized manifolds. For each trajectory we count the number of transitions N_t between the δ-neighborhoods of M_S and M_A, and compute the average intermittent transition duration $\bar{\tau}_t$, defined as the mean time interval separating consecutive visits to these neighborhoods. This interval includes both direct passages from one manifold to the other and excursions that temporarily enter the region outside both. Their dependence on modeling error ε and δ is shown in Fig. 7.

Transitions between the two manifolds are essentially absent for very small perturbations, as indicated in Fig. 7(a), indicating that trajectories remain confined to their initial manifold. As ε increases, the number of transitions grows for more permissive tolerances ($\delta = 10^{-4}$, and 10^{-6}), while remaining nearly zero for strict ones ($\delta = 10^{-14}$, 10^{-12}, and 10^{-10}). This behavior reflects the fact that, under larger perturbations, trajectories begin to wander near the boundaries used to classify manifold proximity, leading to frequent reassignments when δ is large, but to almost no crossings when δ is small and most of the dynamics occurs outside both manifolds.

For the specific coupling strength $\kappa = 1.00$, where the attractors exhibit maximal transverse stability, the invariant manifolds are more resilient to perturbations. This increased stability makes it harder for trajectories to leave the neighborhoods of M_S and M_A, resulting in a lower overall number of transitions compared to the $\kappa = 0.41$ case presented here.

The average intermittent duration $\bar{\tau}_t$ exhibits a characteristic non-monotonic dependence on ε, seen in Fig. 7(b). When $\varepsilon \ll \delta$, transition times are long. As ε approaches the tolerance threshold, the durations decrease sharply, reaching a well-defined minimum near $\varepsilon \approx \delta$. Beyond this point, the durations increase again and eventually settle into a plateau once ε exceeds δ by roughly two orders of magnitude.

This dip recovery plateau structure appears consistently for all δ, differing only in the horizontal position of the minimum, which shifts according to the tolerance. Overall, the results show that intermittent transitions are longest when the perturbation is far below or far above the tolerance threshold, and shortest when the two scales are comparable. The same qualitative behavior was also observed for other coupling strengths (e.g., $\kappa = 1.0$) and for different initial condition grids, but these results are not shown here for brevity. Although the absolute magnitudes change, the dependence of the transition duration on ε and δ remains entirely consistent across parameter regimes.

Taken together, the results show that the synchronized and antisynchronized manifolds respond in very different ways to modeling uncertainty. The synchronized manifold remains comparatively robust, and both the time spent near M_S and the fraction of trajectories classified within it decrease only gradually as the perturbation grows. Transitions away from M_S also remain uncommon unless the tolerance δ is sufficiently permissive. The antisynchronized manifold behaves quite differently. Once the modeling error becomes comparable to the classification threshold, that is, when $\varepsilon \approx \delta$, trajectories are quickly expelled from the vicinity of M_A. Its residence times collapse, and the set of initial conditions remaining near it becomes essentially empty.

Overall, the coupled Lorenz-like system displays a coherent and parameter-independent organization. Synchronization remains the most resilient structure under modeling uncertainty, antisynchronization is rapidly destabilized as soon as ε approaches the classification tolerance δ, and the trajectories gradually migrate toward the region outside both invariant structures as the modeling error increases. This behavior reflects, in continuous time, the same qualitative mechanisms observed in the modified Kan map, while exhibiting a distinct hierarchy of robustness between the two invariant manifolds.

Despite the substantial differences between the modified Kan map and the coupled Lorenz-like flow, one being a two-dimensional discrete system and the other a six-dimensional continuous-time model, the same organizing mechanism governs their response to

bounded modeling errors. In both cases, the interplay between perturbation amplitude and classification tolerance produces a robust phenomenology in which trajectories persist near the invariant sets when $\epsilon \ll \delta$, switching activity becomes maximal when ϵ is a few orders of magnitude smaller than δ, permanence collapses when $\epsilon \approx \delta$, and the region outside all invariant structures becomes partially or, in the case of the modified Kan map, even fully occupied when $\epsilon \gg \delta$. This correspondence demonstrates that the essential features of riddling under modeling uncertainty transcend the specifics of the underlying model.

4. Conclusions

In this work, we investigated how a bounded random perturbation affects the dynamics of discrete and continuous-time systems characterized by intermingled basins of attraction. By conducting a comparative investigation between a modified Kan map and a coupled Lorenz-like system, we established that the impact of modeling uncertainty is governed not by the absolute perturbation intensity ϵ but by its magnitude in relation to the classification tolerance δ. This ratio determines the dynamical relevance of the invariant structures, leading to persistence when ϵ remains significantly smaller than δ and, conversely, a sharp collapse of residence times alongside a redistribution of basins when ϵ approaches the scale of δ.

The robust behavior characterized by persistence, maximal switching, and eventual exclusion appears consistent across both systems despite their profound distinctions in dimensionality, topology, and temporal nature. The shared sequence of events indicates that the riddling of basins under this type of bounded random perturbation constitutes an inherent feature of systems with intermingled structures rather than a model-specific artifact. Furthermore, the analysis identified a clear hierarchy of robustness where the synchronized manifold M_S exhibits relative resilience, whereas the antisynchronized manifold M_A demonstrates pronounced fragility. The latter collapses rapidly as soon as the perturbation amplitude approaches the observational threshold, revealing that even small uncertainties can fundamentally destabilize structures that might otherwise appear stable under ideal noise-free conditions.

These findings carry substantial implications for the interpretation of numerical and experimental data in nonlinear dynamics. They demonstrate that small, bounded uncertainties can effectively reorder dynamical outcomes when they reach the scale of the resolution used to identify state-space features. In practical terms, this result suggests that observed transitions between competing invariant sets, often attributed to intrinsic system behavior, may instead arise as artifacts from the interaction between real-world perturbations and the specific classification criteria used to define proximity to invariant manifolds. This highlights a critical need for caution when interpreting the stability of riddled structures in the presence of even minimal environmental or computational noise.

The present analysis suggests several avenues for further investigation. A natural extension involves the development of adaptive classification schemes that mitigate the reliance on fixed tolerances δ, potentially providing a more reliable and resolution-independent detection of manifold proximity. Moreover, deriving analytical approximations for transversal stability under a bounded random perturbation could provide a firm theoretical foundation for the varying sensitivities observed in structures like M_A in the coupled Lorenz-like system.

CRediT authorship contribution statement

Vitor H.A. Fávaro: Writing – review & editing, Writing – original draft, Visualization, Validation, Methodology, Investigation, Formal analysis, Data curation. **Bruno M. Czajkowski:** Writing – review & editing, Validation, Methodology, Formal analysis. **Ricardo L. Viana:** Writing – review & editing, Validation, Supervision, Software, Resources, Project administration, Methodology, Investigation, Funding acquisition, Formal analysis, Conceptualization.

Declaration of competing interest

The authors declare that they have no known competing financial interests or personal relationships that could have appeared to influence the work reported in this paper.

Acknowledgments

The authors acknowledge financial support from the Coordenação de Aperfeiçoamento de Pessoal de Nível Superior (CAPES, Grant Nos. 88887.954987/2024-00 and 88881.143103/2017-01) and the Conselho Nacional de Desenvolvimento Científico e Tecnológico (CNPq, Grant Nos. 403120/2021-7 and 301019/2019-3).

Data availability

Data will be made available on request.

References

[1] Alexander JC, et al. Riddled basins. Int J Bifurc Chaos 1992;2(4):795–813.
[2] Ashwin P. Attractors stuck on to invariant subspaces. Phys Lett A 1995;209:338–44.
[3] Ott E, et al. Scaling behavior of chaotic systems with riddled basins. Phys Rev Lett 1993;71:4134–7.
[4] Lai Y-C, et al. Riddling bifurcation in chaotic dynamical systems. Phys Rev Lett 1996;77:55–8.
[5] Kapitaniak T, Maistrenko YL, Grebogi C. Bubbling and riddling of higher-dimensional attractors. Chaos Solitons Fractals 2003;17(1):61–6.
[6] Lai Y-C, Grebogi C. Obstruction to deterministic modeling of chaotic systems with an invariant subspace. Int J Bifurc Chaos 2000;10(3):683–93.
[7] Ashwin P, Buescu J, Stewart I. From attractor to chaotic saddle: a tale of transverse instability. Nonlinearity 1996;9(3):703–37.
[8] Ding M, Yang W. Observation of intermingled basins in coupled oscillators exhibiting synchronized chaos. Phys Rev E 1996;54:2489–94.
[9] Kan I. Open sets of diffeomorphisms having two attractors each with an everywhere dense basin. Bull Am Math Soc 1994;31:68–74.
[10] Maistrenko Y, et al. Transverse instability and riddled basins in a system of two coupled logistic maps. Phys Rev E 1998;57:2713–24.
[11] Sommerer JC, Ott E. A physical system with qualitatively uncertain dynamics. Nature 1993;365:138–40.
[12] Ashwin P, Breakspear M. Anisotropic properties of riddled basins. Phys Lett A 2001;280:139–45.
[13] Ott E, et al. The transition to chaotic attractors with riddled basins. Phys D 1994;76(4):384–410.
[14] Viana RL, et al. Riddled basins in complex physical and biological systems. J Comput Interdiscip Sci 2009;1(1):73–82.
[15] Camargo S, Lopes SR, Viana RL. Extreme fractal structures in chaotic mechanical systems: riddled basins of attraction. J Phys: Conf Ser 2010;246(1):012001.
[16] Czajkowski BM, Viana RL. Periodic orbit description of the blowout bifurcation and riddled basins of chaotic synchronization. Chaos Solitons Fractals 2024;184:115003.
[17] Lai Y-C, Grebogi C. Intermingled basins and two-state on-off intermittency. Phys Rev E 1995;52(4):R3313(R)–6(R).
[18] Pereira RF, et al. Periodic-orbit analysis and scaling laws of intermingled basins of attraction in an ecological dynamical system. Phys Rev E 2008;78:056214.
[19] Camargo S, Viana RL, Anteneodo C. Intermingled basins in coupled Lorenz systems. Phys Rev E 2012;85:036207.
[20] Parmenter RH, Yu LY. Riddled behavior of certain synchronized systems. Phys Lett A 1994;189(3):181–6.
[21] Heagy JF, Carroll TL, Pecora LM. Experimental and numerical evidence for riddled basins in coupled chaotic systems. Phys Rev Lett 1994;73(26):3528–31.
[22] Ott E, Sommerer JC. Blowout bifurcations: the occurrence of riddled basins and on-off intermittency. Phys Lett A 1994;188(1):39–47.
[23] Ashwin P, Buescu J, Stewart I. Bubbling of attractors and synchronisation of chaotic oscillators. Phys Lett A 1994;193(2):126–39.
[24] Nakajima H, Y. Ueda. Riddled basins of the optimal states in learning dynamical systems. Phys D 1996;99(1):35–44.
[25] Alexander JC, et al. Intermingled basins for the triangle map. Ergodic Theory Dynam Systems 1996;16(4):651–62.
[26] Neubert MG. A simple population model with qualitatively uncertain dynamics. J Theoret Biol 1997;189(4):399–411.
[27] Kapitaniak T, Maistrenko YL. Chaos, synchronization and riddled basins in two coupled one-dimensional maps. Chaos Solitons Fractals 1998;9(1–2):271–82.
[28] Kapitaniak T, et al. Bifurcations from locally to globally riddled basins. Phys Rev E 1998;57(6):R6253(R)–6(R).
[29] Woltering M, Markus M. Riddled basins of coupled elastic arches. Phys Lett A 1999;260(6):453–61.
[30] Cazelles B. Dynamics with riddled basins of attraction in models of interacting populations. Chaos Solitons Fractals 2001;12(2):301–11.
[31] Rabiee M. The occurrence of riddled basins and blowout bifurcations in a parametric nonlinear system. Phys D 2022;435:133291.
[32] Mazanik AA, et al. Hysteresis and chaos in anomalous Josephson junctions without capacitance. Phys Rev Appl 2024;22(1):014062.
[33] Grebogi C, et al. Shadowing of physical trajectories in chaotic dynamics: Containment and refinement. Phys Rev Lett 1990;65:1527–30.
[34] Poon L, et al. Shadowing in chaotic systems. In: Aizawa Y, Saito S, Shiraiwa K, editors. Dynamical systems and chaos. vol. 2, World Scientific; 1995.
[35] Grebogi C, et al. Shadowability of chaotic dynamical systems. In: Handbook of dynamical systems. vol. 2, Elsevier Science; 2002.
[36] Lai Y-C, Grebogi C, Kurths J. Modeling of deterministic chaotic systems. Phys Rev E 1999;59:2907.
[37] Fávaro VHA, et al. Recurrence-based characterization of model shadowability in the presence of unstable dimension variability. Europhys Lett 2025;152(6):61002.
[38] Elwakil A, Ozoguz S, Kennedy M. Creation of a complex butterfly attractor using a novel Lorenz-Type system. IEEE Trans Circuits Syst I 2002;49:527–33.
[39] Czajkowski BM, Viana RL. Riddled basins of chaotic synchronization and unstable dimension variability in coupled Lorenz-like systems. Chaos 2024;34:093113.
[40] Hofbauer F, Hofbauer J, Raith P, Steinberger T. Intermingled basins in a two species system. J Math Biol 2004;49:293–319.
[41] Costantino RF, Cushing JM, Dennis B, Desharnais RA. Chaotic dynamics in an insect population. Nature 1995;375:227–30.
[42] Costantino RF, Desharnais RA, Cushing JM, Dennis B. Experimentally induced transitions in the dynamic behaviour of insect populations. Science 1997;275:389–91.
[43] Lorenz EN. Deterministic nonperiodic flow. J Atmos Sci 1963;20:130–41.
[44] Sparrow C. The Lorenz equations: Bifurcations, chaos, and strange attractors. Springer; 1982.
[45] Chen G, Ueta T. Yet another chaotic attractor. Int J Bifurc Chaos 1999;9:1465–7.
[46] Ozoguz S, Elwakil A, Kennedy M. Experimental verification of the butterfly attractor in a modified Lorenz system. Int J Bifurc Chaos 2002;12:1627–36.
[47] Elwakil A, Ozoguz S, Kennedy M. A four-wing butterfly attractor from a fully autonomous system. Int J Bifurc Chaos 2003;13:3093–8.
[48] Liu W, Chen G. A new chaotic system and its generation. Int J Bifurc Chaos 2003;13:261–7.
[49] Karnatak R, Ramaswamy R, Prasad A. Amplitude death in the absence of time delays in identical coupled oscillators. Phys Rev E 2007;76:035201.
[50] Yu S, Tang WKS. Tetrapterous butterfly attractors in modified Lorenz systems. Chaos Solitons Fractals 2009;41:1740–9.
[51] Singh JP, Roy BK. Hidden attractors in a new complex generalised Lorenz hyperchaotic system. Nonlinear Dynam 2018;92:373–94.